Nuclear Instruments and Methods in Physics Research A 1057 (2023) 168755

Contents lists available at ScienceDirect

Nuclear Inst. and Methods in Physics Research, A

journal homepage: www.elsevier.com/locate/nima

Full Length Article

Ionoacoustic monitoring of relativistic heavy ion beams

L. Kirsch [a,b,c], W. Assmann [a,*], S. Gerlach [a], A.-K. Schmidt [a], M. Bender [b,d], K. Parodi [a], J. Schreiber [a], C. Trautmann [b,c]

[a] Department of Medical Physics, Ludwig-Maximilians-Universität München, Am Coulombwall 1, 85748, Garching, Germany
[b] Materialforschung, GSI Helmholtzzentrum, Planckstraße 1, 64291, Darmstadt, Germany
[c] Materialwissenschaften, Technische Universität Darmstadt, Peter-Grünberg-Straße 2, 64287, Darmstadt, Germany
[d] Ingenieurwissenschaften, Hochschule RheinMain, Am Brückweg 26, 65428, Rüsselsheim, Germany

ARTICLE INFO

Keywords:
Ionoacoustics
Swift heavy ions
Particle detector
Ultrasonic transducer
Energy determination

ABSTRACT

The performance of ionoacoustic detectors is investigated with respect to application of high-precision range and energy loss measurements for relativistic heavy ions. The technique is based on the generation of a pressure wave when a microsecond-pulsed relativistic ion beam is stopped in a water container. The acoustic signal from individual ion pulses is registered by a piezoelectric detector and analyzed in the time/frequency domain to identify the location of pressure wave generation. The experiments were performed at the SIS18 synchrotron at GSI Helmholtzzentrum (Darmstadt, Germany) with Xe, Pb and U ions of energies between 200 MeV/u and 1 GeV/u. We show that the signal amplitude of the acoustic pressure pulse has a linear correlation with the beam intensity within a range of at least 10^4 to 10^9 particles/spill.

By determining the delay time of the primary and reflected acoustic signal in the water reservoir, the ionoacoustic technique provides information on ion ranges of 1 % accuracy. By an energy-range calibration in combination with a simulation code such as FLUKA, the range data can be used to determine the beam energy. As demonstrated, inserting targets of known thickness in front of the detector is a simple approach for measuring the energy loss of relativistic ions. The advantage of the ionoacoustic technique is the rather simple experimental setup, the huge dynamic range, the information available online by means of only a single pulse and its radiation hardness. Ionoacoustic detectors have great potential as intensity and energy monitor for short-pulsed light and heavy ion beams at existing or future high-energy ion facilities.

1. Introduction

Detectors for high-energy heavy ions are usually based on electronic effects, but rarely on acoustics. The latter possibility was demonstrated many years ago in seminal experiments by Sulak et al. who measured proton pulses by the ion-induced acoustic (*ionoacoustic*) effect in various liquids [1]. Energetic ions slowing down in matter deposit their energy in a characteristic way determined by the charge and velocity of the ions as described by the Bethe-Bloch equation [2]. The energy loss as a function of ion range (Bragg curve) has a maximum (Bragg peak, BP) shortly before the ions come to a complete stop. The energy deposited along the ion trajectory causes heating and expansion of the stopping medium followed by the creation of a pressure wave. Especially at the Bragg maximum the pressure wave can give rise to a characteristic ionoacoustic signal, provided the beam intensity is sufficiently high and concentrated in a short enough ion pulse. The latter condition limits the pulse duration to the time, when the pressure wave leaves the heated region (stress confinement), which requires a pulse length in the microsecond range for relativistic heavy ions. For microsecond pulsed beams, heat diffusion can be neglected (thermal confinement) and the ionoacoustic signal resulting from the temperature gradient delivers spatial and temporal information about the dose deposition. The thermoacoustic method is widely used in photo- or optoacoustics for imaging of tissue. The heat source is created by energy deposition of space- and time-confined laser light [3], with the acoustic wave generation being based on the same physical principles as in ion-induced thermoacoustics [4]. Basic studies on ionoacoustic effects were performed with high-energy protons [1], later followed by applications in different fields such as cosmic neutrino research [5,6], particle therapy [7–10] or laser ion acceleration [11,12]. Ionoacoustic monitoring of GeV heavy ions, also previously proposed in Ref. [1], was studied at the RIKEN cyclotron (Japan) [13], the HIMAC synchrotron (Japan) [14–17] and

* Corresponding author.
E-mail address: walter.assmann@lmu.de (W. Assmann).

https://doi.org/10.1016/j.nima.2023.168755
Received 9 July 2023; Received in revised form 30 September 2023; Accepted 1 October 2023
Available online 16 October 2023

the SIS18 synchrotron of GSI (Germany) using different setups [18]. In the GSI experiment, the ions were stopped in a simple water container equipped with a commercial piezo-composite (lead zirconate titanate, PZT) ultrasound (US) transducer placed on the beam axis. From the PZT registered signal, the range of the ion pulse in the water column is deduced. Despite the simple setup, the signal provided a remarkable precision in range or energy resolution in the permille range and a dynamic intensity range of several orders of magnitude [18].

To further promote the ionoacoustic method for monitoring pulsed heavy-ion beams, this study focuses on the development of more sophisticated and compact detector designs and investigates various techniques for extracting the signal information. The applicability of this novel detection technique to energy loss measurements for GeV ions is demonstrated.

2. Ionoacoustic detector setups

The irradiation experiments were conducted in cave A at the heavy ion synchrotron SIS18 of the GSI Helmholtzzentrum in Darmstadt (Germany). A scheme of the experimental setup is shown in Fig. 1. The pulsed ion beam delivered by the synchrotron is extracted from the vacuum beamline through a 50 µm thick stainless steel window. Inside the beamline, a calibrated SEETRAM (SEcondary Electron TRansmission Monitor) unit consisting of three 12.5 µm thick titanium foils provides information about the intensity and time profile of the ion pulse. The extracted ion beam travels through about 2.1 m of air and then enters the water-filled ionoacoustic setup through a thin Kapton window. The ions are stopped in the water container which is closed in contrast to the open container used in earlier experiments [18]. The back wall of the container is equipped with an ultrasonic transducer positioned on the beam axis. The water is deionized and its temperature is continuously monitored with an accuracy of ±1 K with a PT100 gauge. We tested three different detector designs of increasing complexity to demonstrate possible additional features.

The simplest ionoacoustic setup (design A) consists of a standard 4-way reducer cross (DN 40/16 ISO-KF) equipped with a 75 µm thick Kapton foil as entrance window and an ultrasonic transducer at the opposite end as schematically shown in Fig. 1. The distance between the entrance window and the transducer front side amounts to 98 mm in water. The two vertical DN 16 connections are used for water filling and temperature measurements (Fig. 2, left).

The second setup (design B) is very similar, but here the water column can be adjusted to a variable length to adapt the distance between the Bragg peak position and the transducer to different ion ranges. This is realized by a sliding seal DN 40 ISO-KF tube inside a DN 50 ISO-KF cross moved by a stepping motor from 221 to 294 mm water column length with 10 µm accuracy (Fig. 2, right). This feature also allows for an in-situ measurement of the actual speed of sound by varying the Bragg peak to transducer distance in discrete steps, similarly as demonstrated in Ref. [18].

The third detector I-BEAT 3D (design C) is an advanced version of the I-BEAT (Ion Beam Energy Acoustic Tracing) detector developed originally for the detection of laser accelerated ions [11,12]. It consists of a cubic aluminum water container with a 50 µm thick Kapton entrance window of 20 mm diameter (Fig. 3). The water container has connections for four PZT transducers. In addition to the axial transducer, three lateral transducers are mounted equidistantly aligned to each other, in order to have their focal points overlapping in the center of the detector. The lateral transducers are sensitive to the acoustic waves emitted vertically to the axis of the ion path and, therefore, design C is in principle able to measure the position and beam size in 3D [12]. The presented investigation was limited to a test of the beam position with this new monitor system.

For the I-BEAT 3D detector we used focused ultrasonic immersion PZT transducers (Videoscan, Olympus) with 10 MHz central (sending) frequency and 25.4 mm focal length (Fig. 4, right). In an earlier EIR calibration of this transducer, a frequency response function with a broad maximum around 1.5 MHz was measured with FWHM of about 4 MHz. To enhance the signal amplitude and frequency as much as possible, we used focused transducers and positioned in our experiment the BP maximum within their common foci.

The two other ionoacoustic detectors (design A and B) were equipped with a planar PZT transducer (0.5 or 1 MHz) or alternatively with an immersion hydrophone based on piezoelectric polyvinyldifluoride (PVDF) foils, both types are commercially available. The PVDF based transducer is a circular plane piston hydrophone (ML4X50, Precision Acoustics, UK) containing a 4-layer laminate of 50 µm gold coated PVDF foils (Fig. 4, left). In contrast to PZT transducers, it provides a very broadband frequency response from 50 kHz up to 10 MHz and almost constant sensitivity (typically −216 dB re: 1V/mPa) between 300 kHz and 1 MHz.

The transducer signals were amplified with a low noise broadband, remote controllable voltage amplifier (Femto DHPVA-201), which could be adjusted in 10 dB increments from 10 to 60 dB, depending on the beam intensity. Signals were recorded by a four-channel digitizing oscilloscope (Picoscope 6404D) at a 2.5 GS/s sampling rate. For large enough signal to noise ratios (SNR), data recording could be triggered by the signal itself, but in any case, the SEETRAM produces a clear trigger.

3. Ionoacoustic signal generation and evaluation

3.1. Ionoacoustic signal generation by heavy ions

To briefly explain the general ionoacoustic signal generation the evolution of the energy loss of different 400 MeV/u heavy ions in water as simulated with FLUKA (FLUKA 2021, version 2.3) is shown in Fig. 5 [19]. Bragg curves in Fig. 5 represent exemplary ion species of equal specific energy and thus similar ranges that can be easily displayed on the same x-scale. The normalized 1 GeV/u ^{124}Xe Bragg curve looks not much different, but has a much larger range. According to simulations,

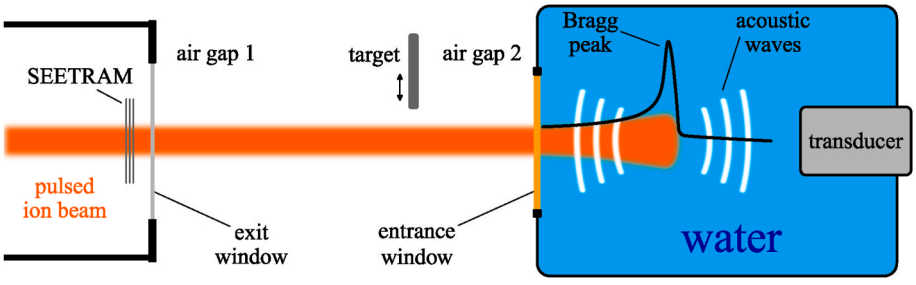

Fig. 1. Schematic of the ionoacoustic setup (not to scale): After passing through the SEETRAM beam monitor, the ion pulse leaves the beamline vacuum through the exit window, travels through about 2.1 m of air and enters the water-filled container through the entrance window. From the energy loss maximum (Bragg peak) an (iono)acoustic signal is emitted, which is registered by the ultrasonic transducer mounted on beam axis. After air gap 1, 1.9 m behind the exit window, a remote-controlled stage allows insertion of targets for energy loss measurements.

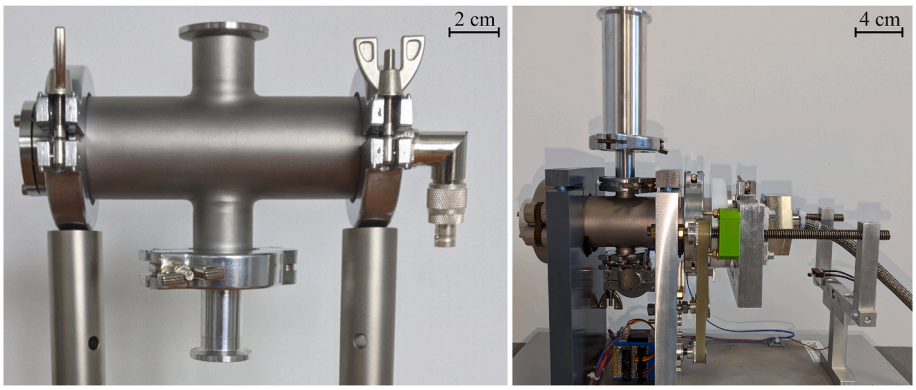

Fig. 2. Ionoacoustic monitor designs: In each setup the ion beam enters the water container from the left through a Kapton window, the axial transducer is mounted on the right flange. (left) In the simplest version (design A), the upper nozzle is used for water filling and the lower nozzle for temperature measurements. (right) In the more advanced version (design B), the water container has a variable length adjusted by a stepping motor with drive belt and spindle. The water reservoir is mounted on top.

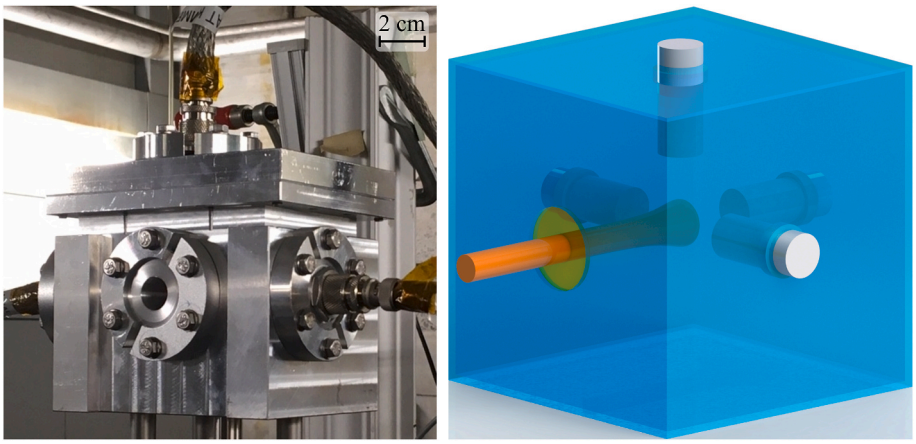

Fig. 3. Photo (left) and schematic (right) of I-BEAT 3D detector (design C). Besides the axial transducer it houses three lateral transducers mounted perpendicular to the beam axis, one on top and two left and right. Ions enter the detector through the entrance window on the front side.

Fig. 4. Immersion transducers used in our ionoacoustic setups: (left) Circular plane piston hydrophone ML4X50 based on gold coated PVDF foils, active diameter 23 mm (Precision Acoustics, Dorchester, UK). (right) Focused PZT transducer, active diameter 13 mm (Videoscan, Olympus, Germany).

primary ions produce the dominant Bragg peak structure at all energies used in this study, which is confirmed by the fact that we did not observe any other signal from reaction products besides the primary ion signal. Nuclear reaction products are either too light or too much distributed in mass and energy to produce more than background noise. In addition to the influence of the temporal beam profile, the strength of the ionoacoustic signal depends crucially on the spatial gradient of the energy deposition, which is most pronounced around the Bragg peak. The acoustic signal seen by an axial transducer therefore originates predominantly from this region of highest energy loss.

The acoustic pressure pulse induced by less than a microsecond long ion bunch is composed of a compression and a rarefaction phase, which is recorded by an ultrasound transducer as a bipolar voltage signal beginning with a positive amplitude [20]. Due to the total impulse response (TIR) of the detector setup (composed of transducer, preamplifier and cables electrical response (EIR) and its spatial impulse response (SIR)), this bipolar signal can undergo phase shifts including a complete inversion of the amplitude from positive-negative to

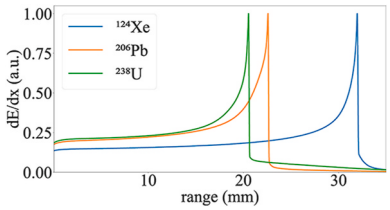

Fig. 5. Energy loss distribution of 400 MeV/u Xe, Pb and U ions in water according to FLUKA simulations. The energy loss of the different ions is normalized to the Bragg peak maximum.

negative-positive. To illustrate the typical bipolar signature of the ionoacoustic signal of a single ion bunch, Fig. 6 presents the signal of 1 GeV/u ^{124}Xe ions together with the time profile of this ion bunch with 340 ns FWHM as measured by the beamline SEETRAM. The three peaks equidistant in time are characteristic for the ionoacoustic signals received by an axial transducer in those setups [18]. The first and most prominent peak (1) originates from the pressure wave created at the Bragg peak position and traveling directly to the transducer. The second, slightly delayed peak (2) is ascribed to the pressure wave created at the entrance window where the ion beam is exposed to a strong energy loss gradient. The third peak (3) is further delayed and is due to the reflection of the pressure wave (1) at the entrance window.

3.2. Signal evaluation in the time and frequency domains

The time difference Δt between the ionoacoustic signal (1) and (2) (cf. Fig. 6) results from the distance between the Bragg peak location where the ultrasonic wave is created and the entrance window. Both waves have a different travel time to reach the transducer. Knowing the temperature dependent speed of sound c_s in water [21], the ion range r can easily be calculated with $r = c_s\,\Delta t$. A second independent method for range determination is the time difference between (1) and (3), because the travel time corresponds to twice the range. As signal (2) is sometimes very weak, the latter approach is usually preferred. To derive the ion range from the transducer signals, their respective time delay has to be determined. For the signals shown in Figs. 6b and 10, this time delay can be deduced from zero-crossings [8]. For signal shapes that are more complicated due to phase shifts or complex ion bunch structures, the evaluation is less straight forward. In those cases, the data evaluation can be performed using a correlation based analysis as shown in Refs. [18,20]. This procedure is also better suited for automated signal evaluation of larger data sets. A complete analysis in the frequency domain has been presented by Wieser et al. [22].

Fig. 7 shows a representative example of a 300 MeV/u ^{238}U ion spill extracted from SIS18 in four micro bunches each with 100 ns FWHM. The signals from the four micro bunches as recorded by the SEETRAM are well separated (Fig. 7a), while the corresponding ionoacoustic signals from the PVDF transducer have a complex waveform due to the partly overlapping contributions from the micro bunches (shown in Fig. 7b including their envelope). By Fourier transformation $\boldsymbol{F}$ of the ionoacoustic time signal $S(t)$, the power spectral density $|\boldsymbol{F}(S(t))|^2$ can be calculated, which is affected here mainly by the SIS18 frequency of the micro bunches (Fig. 7c). By applying appropriate band-pass filters, the SNR of the spectrum can be improved. For the data evaluation here, frequency components below 10 Hz and above 6 MHz were cut off in the power spectrum to remove from $S(t)$ possible DC offset as well as higher frequency noise. Using the signal envelope for the autocorrelation analysis makes the evaluation more robust, insensitive to phase shifts and generally reduces the frequency sensitivity. After band-pass filtering of $S(t)$, the envelope $S_e(t)$ was calculated by Hilbert transformation. According to the Wiener-Khinchin theorem [23], the autocorrelation function $N(t) = \boldsymbol{F}^{-1}\{|\boldsymbol{F}[S_e(t)]|^2\}$, which is obtained by the inverse Fourier transformation $\boldsymbol{F}^{-1}$ of the power spectrum of the envelope of the ionoacoustic signal, finally yields a significant correlation peak corresponding to the time difference between signal (1) and (3) (Fig. 7d). The peak at 16.4 µs marks the best match between the primary (1) and the reflected peak (3) and corresponds to twice the range dependent ultrasound travel time. To summarize, the data evaluation starts from a signal in the time domain, transfers it into the frequency domain for band-pass filtering and after back projection into the time domain performs an autocorrelation analysis of the filtered signal envelop. This procedure was implemented into a software package for online data evaluation of energy and intensity determination.

4. Experimental results

All ionoacoustic experiments were performed at the heavy ion synchrotron SIS18 with ^{124}Xe, ^{206}Pb and ^{238}U ions of energies between 200 MeV/u and 1 GeV/u delivered with an energy uncertainty of $\Delta E/E = 10^{-3}$. According to FLUKA simulations, these energies cover an ion range in water from about 5 mm to 13 cm. The ion beam was typically focused to a spot of about 7 mm FWHM at the entrance window of the water container. For all measurements, the fast extraction mode had to be applied producing a spill length below 1 µs. This is short enough to ensure thermal and stress confinement for the emission of a sharp ionoacoustic wave [24]. Spills produced by fast extraction from SIS18 consisted of up to four micro-bunches of 100 ns length each. Alternatively, extraction after rebunching provided a single ion bunch of 350 ns FWHM, shown in Fig. 6a with about 10^6 particles/spill. All data presented are mean values from 20 to 50 separate consecutive measurements for improved statistics.

4.1. Beam intensity measurements and calibration

For a given setup and fixed ion energy, the amplitude of the ionoacoustic signal is expected to depend only on the number of ions. This

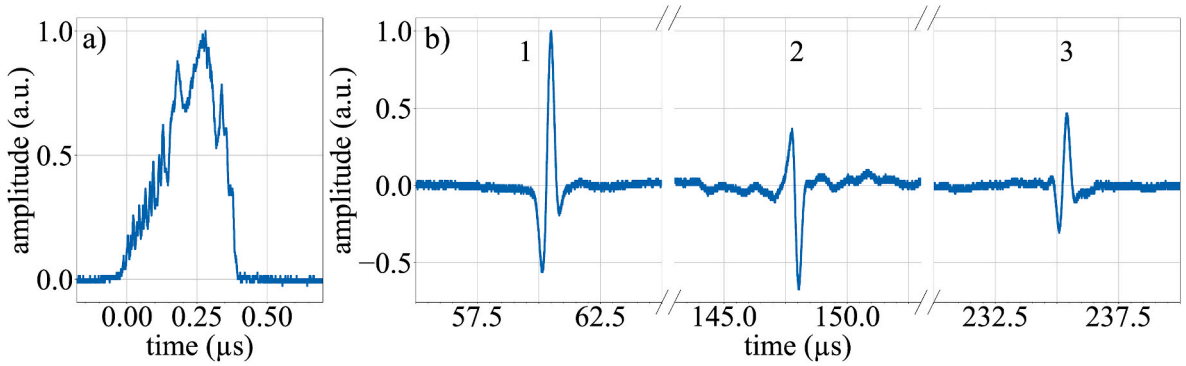

Fig. 6. Trigger and ionoacoustic signals versus time: (a) SEETRAM signal of a single micro bunch (350 ns FWHM) of 1 GeV/u ^{124}Xe ions with 1.3×10^7 particles/spill, (b) normalized axial PVDF transducer signals of ion bunch from (a) showing a peak to peak distance of 340 ns for signal (1). Note the breaks in the time axis.

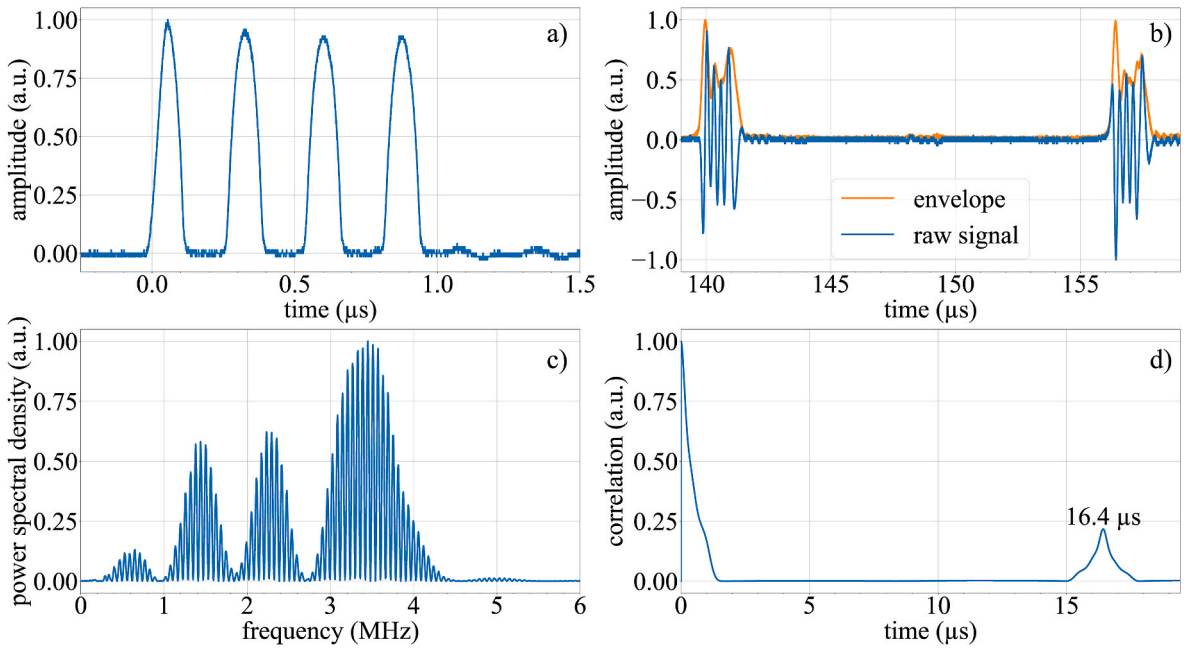

Fig. 7. Normalized experimental and calculated spectra of a single spill with 4 micro bunches of 300 MeV/u ^{238}U ions: (a) SEETRAM signal with well separated micro bunches of 100 ns FWHM each, (b) corresponding PVDF transducer signal *S(t)* (blue) and signal envelop (orange), (c) spectral power density of *S(t)* with cut off frequency at 6 MHz, (d) autocorrelation spectrum *N(t)* from filtered envelope $S_e(t)$ of *S(t)* back projected from (c) (see also text).

correlation is verified with 500 MeV/u ^{206}Pb ions by varying the beam intensity from 2×10^6 to 4×10^7 ions/spill. In this intensity range, the SEETRAM has a calibrated accuracy of 5 %. For this and the following experiments we used detector design B equipped with a planar 1 MHz PZT transducer, but tests with detector design A and a PVDF transducer delivered similar results. Due to the complex ionoacoustic signal from in this case three micro-bunches (Fig. 8a), the envelope integral was used for comparison with the likewise integrated SEETRAM signal. Plotting the ionoacoustic signal versus the SEETRAM signal from single spill measurements (Fig. 8b) shows a strong linear correlation with $R^2 = 0.99$. The ionoacoustic signal could be recorded even below the SEETRAM threshold of about 10^5 particles per spill and quantified by linear extrapolation. We could not test the correlation at higher beam intensities because during this beamtime, the number of particles per spill was limited to 4×10^7.

4.2. Range measurements and energy calibration

Knowing the energy of the ions extracted from SIS18, a range-energy calibration can be performed for a fixed setup to determine unknown energies by extrapolation or interpolation. An example of such a calibration is shown in Fig. 9 with ^{238}U ions of energies between 200 and 400 MeV/u. The range values from the ionoacoustic signals were extracted by autocorrelation analysis of the signal envelopes (cf., Fig. 7). Another example is shown in Fig. 9 for ^{124}Xe ions covering higher energies from 400 MeV/u to 1 GeV/u. These ion ranges were evaluated by zero-crossing analysis of primary and reflected signals (Fig. 6b) and were in agreement with an additional autocorrelation analysis. The main experimental error in the range calculation is caused by the ±1 K temperature inaccuracy of the water container and accounts for 0.2 %, which is smaller than the size of the data symbols in Fig. 9. Mean

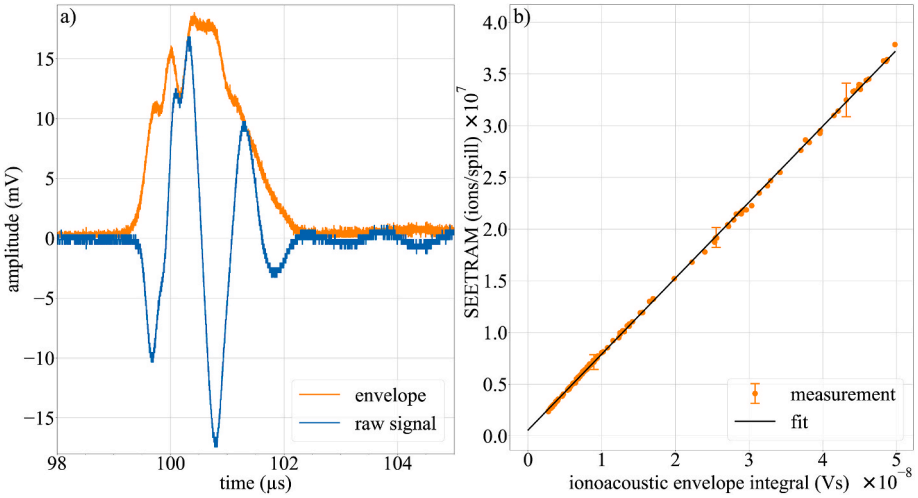

Fig. 8. (a) Primary ionoacoustic signal from a single spill with 2×10^7 particles of 500 MeV/u ^{206}Pb ions, recorded with a planar 1 MHz PZT transducer without amplification. (b) Envelope integral of signal shown in (a) versus beam intensity as measured with SEETRAM. The solid line illustrates the excellent linear correlation within the intensity range from 2×10^6 to 4×10^7 particles/spill.

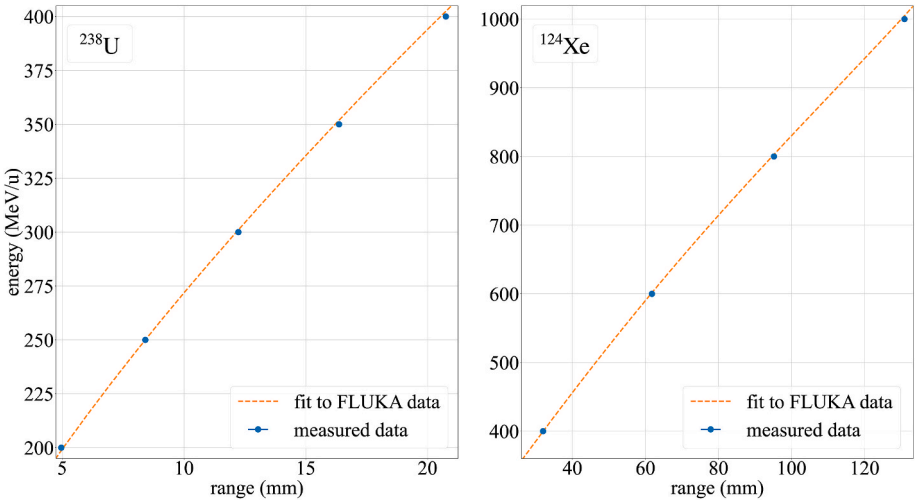

Fig. 9. Energy-range calibration for ^{238}U (left) and ^{124}Xe (right): measured data points (blue) compared to a polynomial fit on FLUKA simulations. Experimental error bars are within data symbols.

standard deviations of repeated measurements were negligibly at 0.01 %. The experimental ranges at the different beam energies are compared with simulated FLUKA ranges (defined by the Bragg peak maximum) considering the energy losses within the entire setup (windows and air gap) (Fig. 9). The error of the FLUKA simulation depends crucially on the input accuracy. In our setup, the air gap between the exit window of the beamline and the entrance window of the detector of 213 cm with an inaccuracy of ±2 cm mainly contributes to the 1 % range uncertainty. The maximum range difference between FLUKA and ionoacoustically measured ranges is 0.18 mm (0.9 %) for ^{238}U ions at 400 MeV/u, which is within the estimated error margins.

4.3. Beam position measurements

To measure the lateral beam position, we used the I-BEAT 3D setup (detector C) equipped with three lateral and one axial focused 10 MHz PZT transducers with focal length of 25.4 mm. ^{238}U ions were selected with an energy of 205 MeV/u calculated by FLUKA and a time profile similar to Fig. 7a. The energy was chosen such that the Bragg peak is positioned in the focus of the lateral transducers (see Fig. 3) and, therefore, dominates the ionoacoustic signals. Due to the symmetric transducer arrangement, any beam misalignment would cause a different signal delay at the transducers, which can be directly related to an offset from the detector center. Fig. 10 presents the ionoacoustic signals from all three lateral transducers with measured offsets demonstrating a position resolution as high as 0.1 mm. In Fig. 3, the Bragg peak is placed in the detector center, at the same distance to all four transducers, where also their foci coincide. Due to the time shifts shown in Fig. 10, the actual Bragg peak position is shifted to the left lateral transducer by 6.1 mm and downwards by 6.6 mm.

However, this resolution can only be achieved, if the position of the Bragg peak is within the focal width of the lateral transducers, so that the high frequency components of the ionoacoustic signals can be used for position determination. The proper Bragg peak position was verified within 1.2 mm by evaluation of the axial transducer signal, which is also shown in Fig. 10. The horizontal offset of 6.1 mm was confirmed by GafChrom film measurement at the entrance window with an accuracy of ±1 mm. Note the phase change of 180° between the left and right transducer signals due to the distance sensitivity of the total impulse response of the transducers around their focal point. In this

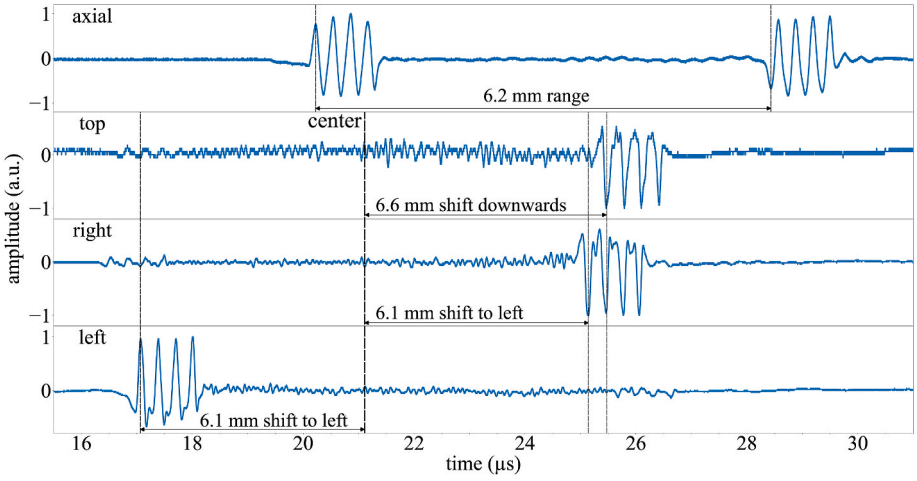

Fig. 10. Ionoacoustic signals of 4 micro-bunches of 205 MeV/u ^{238}U recorded with the I-BEAT 3D detector equipped with three lateral transducers. The position information is deduced from the time shift (offset) from the detector center. Here the lateral beam position is horizontally shifted by 6.1 mm to the left and vertically 6.6 mm downwards. The time shifts are marked on the corresponding maxima and minima for better visibility, the beam position was evaluated by the signal zero crossings (phase shifts are explained in text). The axial transducer signal is shown for comparison, it was used to verify the longitudinal Bragg peak position within the lateral transducer foci.

measurement, the Bragg peak position was horizontally out of center by 6.1 mm towards the left transducer and therefore inside its focal point, i. e. at a distance of 19.3 mm from the transducer surface. Consequently, the Bragg peak position is outside the focal point of the right transducer, which causes the observed phase shift. This interesting feature of a focused transducer is also responsible for equal signal phase of the right and top transducer, in both cases the Bragg peak is positioned outside their focal points.

4.4. Energy loss measurements

Previous experiments with GeV heavy ions and axial transducer geometry have demonstrated that the ionoacoustic method provides range measurements with submillimeter position resolution [18]. This high precision translates directly into an energy resolution below 1 % for GeV heavy ions and offers a simple method for energy loss measurements. Although our experimental setup was not optimized for such a study, we tested this option by placing various materials in front of the ionoacoustic detector and recorded the time shift and, hence, ion range change in the water container with and without a target in the beam (Fig. 11). The determination of the total energy loss of the inserted target, requires the range-energy calibration shown in Fig. 9. As shown in Table 1, the energy loss in the large air gap (air gap 1, see Fig. 1) from the beam exit window to the target cancels out, whereas the energy loss in the air gap between target and detector (air gap 2, see Fig. 1) and in the detector entrance window does not. As a consequence, the target-related range shift is changed by a corresponding offset, which limits the achievable accuracy. The problem can be mitigated by minimizing air gap 2.

We measured the respective range shift with and without the target in the beam for several beam energies and for different materials and thicknesses as shown in Fig. 12 and Table 1. The experimental error for this range-difference measurement is composed of the standard deviation for repeated range shift measurements (±3 μm) and the temperature inaccuracy (±1 K). Both errors decrease with increasing range shift. Fig. 12 compares the experimental results with FLUKA simulations using the ion energies at the target entrance. As for the experiment, most of the input errors cancel out in the simulation, except for the target thickness inaccuracy, which amounts to 2 % of the calculated energy loss of the Kapton film (74.7 ± 0.3 μm) and 5 % for the other targets. An additional error is caused by the simulation grid size of 4 μm which further limits the accuracy of the calculation. Within these uncertainties, the experimental data and the FLUKA simulations are in full agreement.

For very thin targets, the time resolution of the ionoacoustic detector may become the limiting factor for energy loss measurements. Taking the 66 ns time shift for a 75 μm thick Kapton foil as shown in Fig. 11 and the sound velocity in water of 1.5 mm/μs, a range shift of 100 μm can be easily measured, which corresponds for 250 MeV/u ^{238}U with about 8.3 mm range in water to a range resolution of about 1 %. Translated into energy resolution, the time shift in Fig. 11 is related to 306 MeV energy loss of 59500 MeV ^{238}U ions in 75 μm Kapton yielding 0.5 % resolution.

Knowing the beam energy before and after the target from FLUKA, the energy lost in the target can be divided by the respective target thickness yielding the mean energy loss. At relativistic energies, the energy loss as a function of energy is rather flat and, therefore, the variation in energy loss within thin targets is small. Our energy loss measurements for several materials and thicknesses are collected in Table 2, confirming FLUKA values and being again in high accordance within the noted error margins.

5. Discussion and outlook

In contrast to the few previous ionoacoustic investigations with relativistic heavy ions in Japan at RIKEN [13] and HIMAC [14–17], our detector system uses only one single standard transducer placed downstream on the beam axis. With this rather simple setup an energy resolution in the permille range could be demonstrated. In the extensive series of experiments at HIMAC with 400 MeV/u Xe ions in different liquids up to 14 special ring-shaped PZT transducers were used which were mainly sensitive to the lateral ionoacoustic signal. However, the intensity as well as energy and position of the beam were difficult to extract quantitatively from these experiments. Our geometry has the advantage that the accuracy of the extracted ion range and intensity is much better, if the Bragg peak position is in the far field regime of the transducer [18]. Furthermore, transducers with various frequency characteristics are available commercially according to the experimental requirements, based either on PZT or PVDF.

We observe a strict linear correlation between the number of ions in a beam pulse and the signal amplitude of the acoustic pressure pulse (Fig. 8b). Our experiments covered an intensity range from 10^4 to 10^9 particles/spill, but the linearity is most probably preserved at even higher intensities. Depending on the beam focus, for a spot size of few mm^2 no saturation effects are expected for heavy ions of at least 10^{10} particles. Regarding the sensitivity at low intensities, a clear ionoacoustic signal was measured in a previous experiment for a single spill of down to only 200 U ions [18]. We are therefore confident in extrapolating the calibration fit in Fig. 8b by two orders of magnitude on both sides. Accordingly, this ionoacoustic detector covers a linear regime from 10^2 to 10^{10} particles/spill which is unusually large compared to electronic particle detectors. Moreover, ionoacoustic detectors do not suffer from radiation damage because the detection medium is not a solid but a liquid (water). Yet, activation of detector components including water was observed after accumulation of a high dose, but this did not affect the measurement accuracy.

Besides its application as beam intensity monitor, the ionoacoustic technique also provides information on ion ranges in water. We compared FLUKA simulations with range values measured at specific energies and can confirm excellent agreement. The accuracy is limited by energy losses in components along the beamline such as beam windows and air gaps. An energy-range calibration of the ionoacoustic monitor can be performed in two ways: either by a fit of range measurements at different beam energies, or by calculating the energy-range

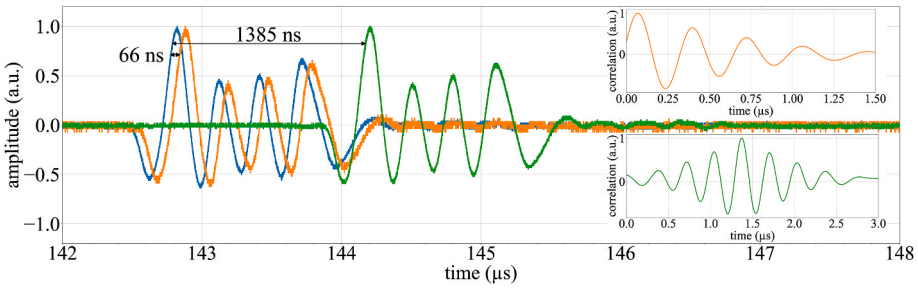

Fig. 11. Primary signal with time shift of a spill of 250 MeV/u ^{238}U ions before (blue) and after inserting a 75 μm Kapton foil (orange) or a ~ 1 mm thick aluminum plate (green) in front of the ionoacoustic detector. The related range shifts correspond to respective energy losses of 306 MeV and 6923 MeV, which is 0.5 % and 12 % of the initial total energy. Insert: correlation analysis, maximum correlation of 1.0 corresponds to the energy loss related time shift.

Table 1
Energy loss (in MeV) due to contributions of different elements along the path of 300 MeV/u (71400 MeV) ^{238}U ions according to FLUKA simulations, without (none) and with different targets inserted into the beam. Setup adjusted to 191 cm for air gap 1 and 22 cm for air gap 2 (see Fig. 1).

Target	Thickness (μm)	SEETRAM (MeV)	Beam exit (MeV)	Air gap 1 (MeV)	Target (MeV)	Air gap 2 (MeV)	Det. Entrance (MeV)	Water (MeV)
none		318.5	770.4	5259.5	0	620.5	269	64162.1
Energy difference compared to data without target								
Kapton	75	0	0	0	265.1	6.6	1.0	−272.5
Au	79	0	0	0	2472.8	22.6	6.5	−2501.8
Ta	101	0	0	0	2784.8	24.6	7.3	−2816.7
Al	969	0	0	0	6269.9	47.8	16.0	−6333.7

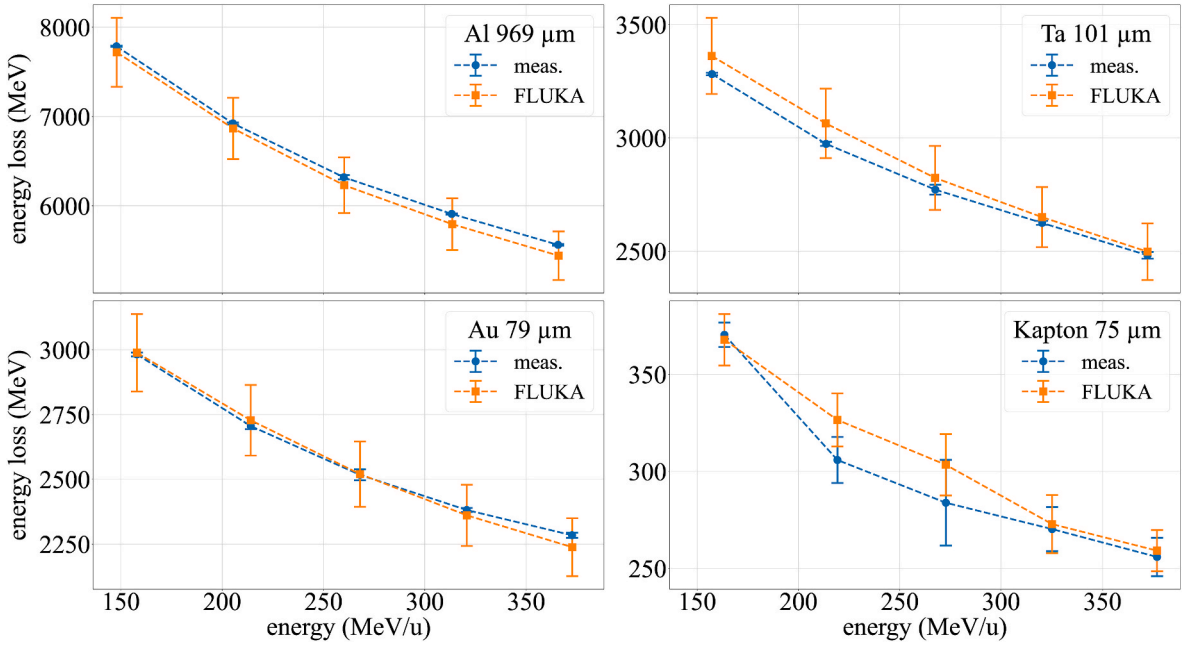

Fig. 12. Energy loss measurements with ^{238}U ions of mean energy within the targets for four different targets compared with FLUKA simulations (see also text). Energy error bars are within data symbols.

curve with FLUKA and implementing the experimental range at one specific energy to the FLUKA curve. Ionoacoustic range data, possibly in combination with FLUKA, thus offer a simple and precise method in determining the energy of relativistic ion beams.

Using a detector design with a variable water column, the measurable range can cover heavy ion energies from 100 MeV/u to 10 GeV/u. For even higher energies, the ionoacoustic detector could be modified to a transmission mode with lateral transducers only and the axial transducer replaced by an exit window. This design delivers also information about the beam intensity, but primarily monitors the lateral beam position. The latter was tested with I-BEAT 3D demonstrating that the radially emitted acoustic signal from the Bragg peak yields a similar submillimeter resolution of the beam position as with the axial transducers [12]. As pointed out in section 4.3, this lateral position resolution required adjusting of the Bragg peak into the plane of the lateral transducers, which could be obtained and verified by the axial transducer signal. The submillimeter lateral position resolution could be of real use for strongly collimated heavy ion beams.

It should be emphasized, that the achievable resolution of ionoacoustic range measurements does not depend on the signal frequency as in ultrasound imaging, where the spatial resolution degrades from submillimeter for MHz frequencies to many millimeters in the kHz range. Unlike ultrasound imaging, where the separation of two objects is limited by the sound wavelength, ionoacoustics only requires the identification of the position of the Bragg peak maximum, which depends on the time resolution of the transducer. For relativistic ion energies, the frequency determining width of the Bragg peak is some millimeters, thus the mean acoustic signal frequency is in range of 1 MHz. However, this does not affect the range and energy resolution, both are even improving with increasing ion energy.

An obvious application of the ionoacoustic technique is the measurement of the energy loss of relativistic ions, for which only scarce data are available in literature. Our range measurements with and without a specific target provide a simple experimental approach to energy loss values with an uncertainty of less than 1 %. Even better accuracy can be achieved if the ionoacoustic detector is positioned as close as possible to the exit window of the beamline, thus minimizing additional energy losses outside the target.

In summary, tests with various monitor designs have demonstrated that the ionoacoustic technique provides a rather simple method for analyzing beam properties of microsecond-pulsed relativistic heavy ions. Even the simplest setup using an axially mounted standard transducer delivers information on beam intensity and energy with few percent uncertainty. Adding three lateral transducers extends the capabilities of this ionoacoustic monitor to determine the beam position with submillimeter resolution. So far, no saturation effects have been seen up to 10^9 ions per spill. The detectors suffer no radiation damage and could be suitable as a second generation “Faraday cup” at existing or upcoming GeV heavy ion facilities [25].

Declaration of competing interest

The authors declare that they have no known competing financial interests or personal relationships that could have appeared to influence

Table 2
Energy loss data from ionoacoustic measurements with ^{238}U ions for various materials and thicknesses compared to FLUKA simulations. Ion exit energy as delivered by SIS18. (see also text).

Target		Ion exit energy	Mean energy in target	Measured dE/dx	FLUKA dE/dx	Δ dE/dx FLUKA - measured
Material	Thickness μm	MeV/u	MeV/u	MeV/μm	MeV/μm	MeV/μm
Kapton	75	200	163.47	4.96 ± 0.30	4.93 ± 0.40	−0.03
		250	219.23	4.10 ± 0.34	4.37 ± 0.38	0.27
		300	272.74	3.80 ± 0.47	4.06 ± 0.40	0.26
		350	325.14	3.62 ± 0.31	3.65 ± 0.38	0.03
		400	376.91	3.43 ± 0.28	3.47 ± 0.30	0.04
Al	968.7	200	147.88	8.04 ± 0.43	7.97 ± 0.86	−0.07
		250	205.33	7.15 ± 0.39	7.09 ± 0.76	−0.06
		300	260.05	6.52 ± 0.37	6.43 ± 0.69	−0.09
		350	313.29	6.1 ± 0.33	5.98 ± 0.63	−0.12
		400	365.76	5.74 ± 0.31	5.62 ± 0.6	−0.13
	6062.7	350	237.64	6.91 ± 0.37	6.97 ± 0.81	0.06
		400	297.1	6.31 ± 0.33	6.33 ± 0.72	0.02
Ta	101	200	157.34	32.34 ± 1.76	33.13 ± 3.49	0.79
		250	213.62	29.3 ± 1.64	30.2 ± 3.2	0.89
		300	267.5	27.31 ± 1.66	27.82 ± 2.94	0.51
		350	320.19	25.86 ± 1.45	26.12 ± 2.76	0.25
		400	372.23	24.46 ± 1.44	24.61 ± 2.47	0.16
	238.4	250	204.9	29.89 ± 1.61	30.8 ± 3.29	0.91
		300	259.48	27.64 ± 1.54	28.27 ± 3	0.63
		350	312.64	26.08 ± 1.42	26.46 ± 2.81	0.38
		400	365	24.84 ± 1.37	24.99 ± 2.65	0.15
Au	153.2	200	157.97	37.61 ± 2.08	37.69 ± 3.95	0.08
		250	214.19	34.12 ± 1.95	34.41 ± 3.6	0.28
		300	268.04	31.75 ± 1.95	31.79 ± 3.38	0.04
		350	320.7	30.03 ± 1.68	29.78 ± 3.24	−0.26
		400	372.64	28.81 ± 1.65	28.23 ± 2.96	−0.58
	365	250	206.45	33.79 ± 1.83	34.91 ± 3.73	1.12
		300	260.93	31.23 ± 1.75	32.09 ± 3.41	0.87
		350	313.97	29.54 ± 1.61	30.08 ± 3.19	0.55
		400	366.25	28.18 ± 1.55	28.4 ± 3.02	0.23
	1333.3	350	232.7	33.2 ± 1.76	33.84 ± 3.86	0.64
		400	291.69	30.59 ± 1.62	31.13 ± 3.53	0.54
SiO_2	1771.6	250	194.66	6.77 ± 0.36	6.87 ± 0.75	0.10
		300	250.52	6.13 ± 0.34	6.18 ± 0.67	0.06
		350	304.57	5.68 ± 0.3	5.71 ± 0.61	0.04
		400	357.52	5.35 ± 0.29	5.36 ± 0.57	0.01

the work reported in this paper.

Data availability

Data will be made available on request.

Acknowledgement

The results presented here are based on the SMAT experiments, which were performed in cave A at SIS18 at the GSI Helmholtzzentrum für Schwerionenforschung, Darmstadt (Germany) in the frame of FAIR Phase-0. This work has been supported by GSI as part of the R&D project GSI-LMASS1821 with the Ludwig-Maximilians-Universität München. SG received financial support by the German Research Foundation (DFG) within the Research Training Group GRK 2274. AS was supported by GSI within the R&D project GSI-LMSCH2025 with the Ludwig-Maximilians-Universität München.

References

[1] L. Sulak, et al., Experimental studies of the acoustic signature of proton beams traversing fluid media, Nucl. Instrum. Methods 161 (2) (1979) 203–217.
[2] P. Sigmund, Particle Penetration and Radiation Effects. Springer Series in Solid State Sciences, vol. 151, Springer-Verlag, Berlin Heidelberg, 2006, 3-540-31713-9.
[3] L.H.V. Wang, S. Hu, Photoacoustic tomography: in vivo imaging from organelles to organs, Science 335 (2012) 1458–1462.
[4] L.H.V. Wang, Hsin-i Wu, Biomedical Optics: Principles and Imaging, John Wiley & Sons, Inc., 2007.
[5] R. Nahnhauer, Acoustic particle detection – from early ideas to future benefits, Nucl. Instrum. Methods Phys. Res., Sect. A 662 (2012) S20–S23.
[6] R. Lahmann, Acoustic detection of high energy neutrinos in sea water: status and prospects, EPJ Web Conf. 135 (2017), 06001.
[7] Y. Hayakawa, et al., Acoustic pulse generated in a patient during treatment by pulsed proton radiation beam, Radiat. Oncol. Invest. 3 (1) (1995) 42–45.
[8] W. Assmann, et al., Ionoacoustic characterization of the proton Bragg peak with submillimeter accuracy, Med. Phys. 42 (2) (2015) 567–574.
[9] K.C. Jones, et al., Experimental observation of acoustic emissions generated by a pulsed proton beam from a hospital-based clinical cyclotron, Med. Phys. 42 (12) (2015) 7090–7097.
[10] S. Lehrack, et al., Submillimeter ionoacoustic range determination for protons in water at a clinical synchrocyclotron, Phys. Med. Biol. 62 (17) (2017) L20–L30.
[11] D. Haffa, et al., I-BEAT: ultrasonic method for online measurement of the energy distribution of a single ion bunch, Sci. Rep. 9 (2019) 6714.
[12] S. Gerlach, et al., Three-dimensional acoustic monitoring of laser-accelerated protons in the focus of a pulsed-power solenoid lens, high power laser science and engineering, High Power Laser Science and Engineering 11 (2023) e38.
[13] T. Kambara, et al., Detection of acoustic signals induced by heavy-ion impact: ion-beam seismology, Nucl. Instrum. Methods Phys. Res., Sect. B 230 (1–4) (2005) 601–607.
[14] T. Miyachi, et al., Acoustic response of piezoelectric lead–zirconate–titanate to a 400MeV/n Xenon beam, Jpn. J. Appl. Phys. 42 (2003) 1456–1457.
[15] T. Miyachi, et al., Response of acoustic signals generated in water by energetic xenon ions, Nucl. Instrum. Methods Phys. Res., Sect. A 560 (2) (2006) 606–612.
[16] S. Takechi, S. Morinaga, A. Kurozumi, T. Miyachi, M. Fujii, N. Hasebe, H. Shibata, T. Murakami, Y. Uchihori, N. Okada, Detection of high-energy heavy ions using piezoelectric lead zirconate titanate, J. Appl. Phys. 105 (2009), 084903.
[17] M. Kobayashi, T. Miyachi1, O. Okudaira, S. Takechi, A. Kurozumi, T. Uno, M. Nakamura, H. Shibata, N. Okada, M. Fujii, T. Murakami, Y. Uchihori, Acoustic

signal production in ethanol by energetic xenon ions, Jpn. J. Appl. Phys. 59 (2020), 028004.
[18] S. Lehrack, et al., Ionoacoustic detection of swift heavy ions, Nucl. Instrum. Methods Phys. Res., Sect. A 950 (2020), 162935.
[19] G. Battistoni, et al., Overview of the FLUKA code, Ann. Nucl. Energy 82 (2014) 10.
[20] J. Schauer, et al., Proton beam range verification by means of ionoacoustic measurements at clinically relevant doses using a correlation-based evaluation, Front. Oncol. 12 (2022), https://doi.org/10.3389/fonc.2022.925542.
[21] W. Marczak, Water as a standard in the measurements of speed of sound in liquids, J. Acoust. Soc. Am. 102 (5) (1997) 2776–2779.
[22] H.P. Wieser, et al., Experimental demonstration of accurate Bragg peak localization with ionoacoustic tandem phase detection (iTPD), Phys. Med. Biol. 66 (24) (2021), 245020.
[23] N. Wiener, Generalized harmonic analysis, Acta Math. 55 (1930) 117–258.
[24] K.C. Jones, C.M. Seghal, S. Avery, How proton pulse characteristics influence protoacoustic determination of proton-beam range: simulation studies, Phys. Med. Biol. 61 (6) (2016) 2213–2242.
[25] M. Durante, et al., Applied nuclear physics at the new high-energy particle accelerator facilities, Phys. Rep. 800 (2019) 1–37.